ACS Photonics

pubs.acs.org/journal/apchd5 Article

Nanoscale Spectroscopy of Dielectric Properties of Mica

Alireza Fali, Sampath Gamage, Marquez Howard, Thomas. G. Folland, Nadeemullah A. Mahadik, Tom Tiwald, Kirill Bolotin, Joshua D. Caldwell, and Yohannes Abate*

Cite This: https://dx.doi.org/10.1021/acsphotonics.0c00951 Read Online

ACCESS | Metrics & More | Article Recommendations | Supporting Information

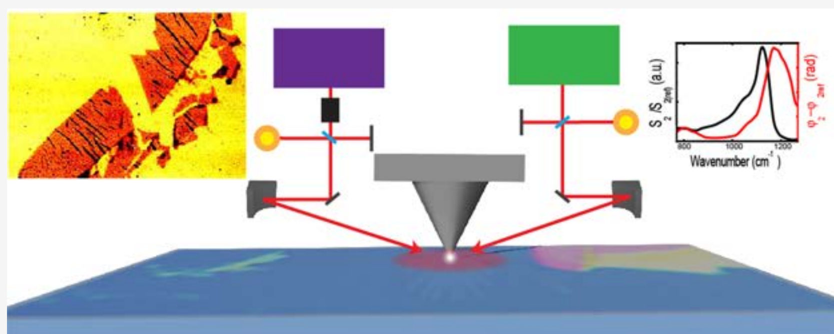

ABSTRACT: Infrared dielectric properties of muscovite mica, one of the first van der Waals crystals, exfoliated on silicon and SiO_2 substrates is studied using near-field nano-FTIR spectroscopy. The spectra of mica show strong thickness and wavelength dependence down to the monolayer-scale, with a prominent broad peak centered around ∼1080 cm^{-1} assigned to stretching vibrations of Si−O. We reveal that the infrared dielectric permittivity of mica is anisotropic, that is, has opposite signs along the in-plane and out-of-plane axes, implying a Type I hyperbolic behavior in the range 920−1010 cm^{-1} and a Type II hyperbolic behavior in the range 1050−1130 cm^{-1}. Experimentally measured nano-FTIR spectra agree well with analytical model calculations based on an extended finite dipole model for layered systems of the tip−sample interaction when the out-of-plane dielectric values (instead of the in-plane dielectric values) were used in the calculations.

KEYWORDS: *hyperbolic materials, mica, 2D materials, nano-FTIR, van der Waals materials*

Since the isolation of monolayer graphene,[1] numerous other layered materials have been identified.[2] These include, transition metal dichalcogenides (TMDs) with the general formula of MX_2, where M is a transition metal atom (e.g., M = Mo, W, Ta, etc.) and X is chalcogen (e.g., X = Se, S, Te) forming layers above and below M, hexagonal boron nitride, and black phosphorus. In addition to providing a unique platform to discover exciting new physics, layered materials are promising for applications in flexible optoelectronics.[3] While the list of metallic and semiconducting 2D crystals is growing by the day, the list of insulating 2D crystals is still limited.

Muscovite mica, with the chemical formula $KAl_2(Al,Si_3)O_{10}(OH)_2$, is among the earliest known van der Waals (vdWs) materials that can be exfoliated in high quality to large sizes (>1 cm^2) with atomic flatness.[4,5] It can be prepared as a monolayer through the exfoliation of natural muscovite.[6,7] The surface unit cell of bulk muscovite mica along the (001) crystal plane harbors two K^+ ions, when exfoliated (along the (001) crystal face), only half the amount K^+ ions per unit cell remain to preserve surface charge neutrality. The K^+ ions are tightly locked in the interlayers, resulting in stronger interlayer force in muscovite mica compared to the weak van der Waals forces between layers in most other 2D materials. On the other hand, the surface K^+ ions exposed during exfoliation of muscovite mica allow unique opportunities for novel surface chemistry due to their ability to exchange with different cationic species and ease of functionalization.[8,9] Because the surface is atomically flat, muscovite mica is an excellent substrate for materials used in optoelectronics such as vdW flakes,[7] self-assembled monolayers,[10−13] and light-emitting devices,[14,15] and is used as a template to produce the active layer in organic solar cells.[16] However, much of the optical properties of a monolayer to few layer mica remain unexplored.

In this work, using a combination of mid-infrared scattering type scanning near-field microscopy (s-SNOM) and nano-FTIR, we perform near-field spectroscopy and imaging of 2D crystal muscovite mica down to the monolayer limit. Ellipsometry measurements enabled the extraction of the

Received: June 14, 2020

© XXXX American Chemical Society

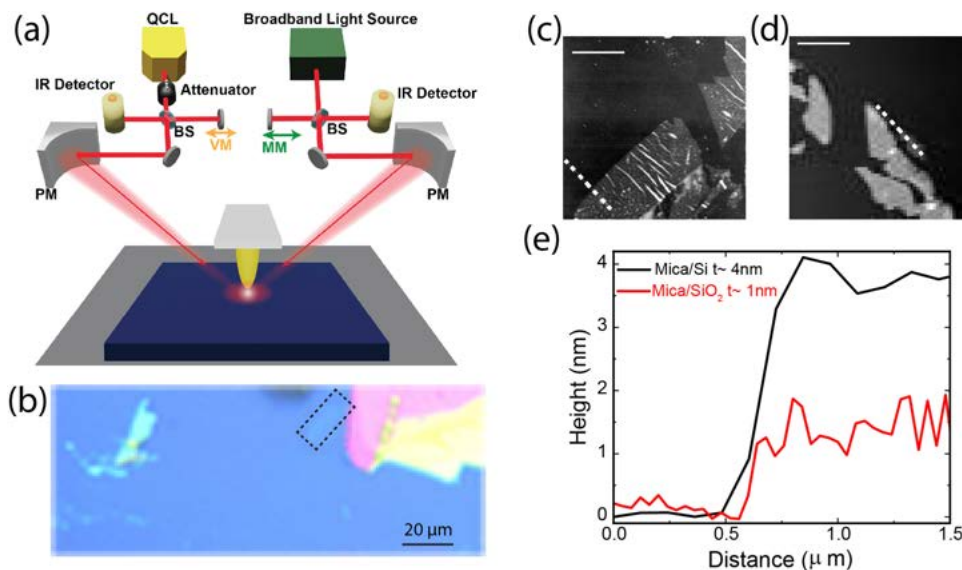

Figure 1. Optical micrograph and AFM topography images of exfoliated muscovite mica flakes. (a) Schematics of the nano-FTIR setup. (b) Optical image of exfoliated mica on SiO_2, Topography and of 4 nm thick mica on Si (c) and 1 nm thick mica on SiO_2 (d) and corresponding height line profiles (e). Scale bars in (c) and (d) are 1 μm.

dielectric function in this spectral range, highlighting that the infrared dielectric permittivity of mica along the ordinary and extraordinary directions have opposite signs in the 920−1130 cm^{-1} range, thus, implying regions of both Type I and Type II hyperbolic behavior. The thickness- and wavelength-dependent IR spectra of muscovite mica exfoliated on either Si or SiO_2 substrates enabled sensitive detection spectra of mica down to the monolayer level, taking advantage of the SiO_2 phonon polariton enhanced resonant excitation. The in-plane and out-of-plane dielectric values of mica extracted from ellipsometry measurements were used to perform model calculations. Good agreement of theoretical calculations with experimentally measured nano-FTIR spectra were achieved when the out-of-plane dielectric values from ellipsometry measurements were used. With reduced loss, mica could provide a robust hyperbolic material for large-scale nanophotonics applications.

■ RESULTS AND DISCUSSION

A commercially available mica sample was used for this study. We performed X-ray diffraction (XRD) measurements on the sample using a Rigaku Smartlab X-ray diffractometer equipped with a 9 kW Cu anode and collimating mirror producing Cu Kα quasi-parallel X-rays. The sample was mounted and aligned on an automated vertical goniometer, and diffraction spectra were collected using a 1d high sensitivity Si strip detector. XRD peak analysis and least-squares refinement were performed to obtain lattice constants, phase orientation, and average grain sizes. The mica sample was found to crystallize in the hexagonal, Muscovite 3T phase with space group: *P*3112. The sample is highly *c*-plane oriented with 7 orders of (00,*l*) reflections observed in the XRD spectra. The spectra also show that the sample has a high crystalline quality within the textured grains. The refined lattice parameters obtained were as follows: $a = 5.1948 \pm 0.0045$ Å and $c = 29.9735 \pm 0.0001$ Å. These XRD spectra and a table containing a list of the observed peaks, along with the indices, the computed peaks of the least-squares refined structure, and differences, as well as further XRD analyses can be found in Figure S1 and Table S1.

A combination of s-SNOM and nano-FTIR is used to acquire topography, near-field images, and IR nanospectra on a muscovite mica sample prepared by mechanical exfoliation on either Si or SiO_2 substrates. The experimental setup ((Figure 1a, neaspec co.) is based on a tapping mode AFM with a cantilevered metal-coated tip that oscillates at a resonance frequency of $\Omega \sim 280$ kHz and a tapping amplitude of ∼50 nm. Either a coherent broadband infrared beam in the frequency range 700−2100 cm^{-1} (for nano-FTIR) or a monochromatic IR laser (for s-SNOM) is focused by a parabolic mirror to the tip. For the nano-FTIR operation, the backscattered near-field light from the tip−sample junction is detected via mixing with an asymmetric Fourier transform Michelson interferometer. This detection method enables recording of both the amplitude $s(\omega)$ and the phase $\varphi(\omega)$ spectra of the backscattered light. To extract background-free, local near-fields, the detector signal is demodulated at a higher harmonic $n\Omega$ of the tip mechanical resonance frequency Ω. Normalized amplitude (s_n(sample)/s_n(reference)) and phase (φ_n(sample) − φ_n(reference)) IR near-field spectra are acquired by first taking the reference spectrum on a reference area (silicon is used in these experiments), followed by taking spectra at desired positions of the sample. Figure 1b shows a representative optical micrograph of mica flakes exfoliated onto a SiO_2 substrate, the rectangular box in black broken lines subtends a monolayer flake. Figure 1c,d shows AFM topography images of mica flakes on SiO_2 and Si, respectively. Red and black lines in Figure 1e are corresponding line profiles taken on dashed lines on the Si substrate (black line) and SiO_2 substrate (red). While we could exfoliate a monolayer (height ∼ 1 nm) flake on SiO_2 substrate,[7] the thinnest flake we could exfoliate on Si had a height of ∼4 nm.

The dielectric function of muscovite mica at mid-IR frequencies is necessary to understand its spectroscopic response, yet has not been reported previously. Thus, we performed ellipsometry measurements in the mid-IR frequency range, using an IR-VASE ellipsometer (J. A. Woollam Co., Lincoln, NE). The substrate was mounted on a precision rotation stage, and a data set was acquired after the substrate

was rotated to 5 different rotational positions around the sample normal −0° (initial position), 45°, 90°, 135°, and 180°. Each data set included of data at incident angles of 45°, 60°, and 75°. All data sets were acquired at a spectral resolution of 8 cm^{-1}. After the measurement, the data were fit to a biaxial substrate model using standard numerical analysis methods similar to those described by Jellison[17−19] and Herzinger.[20] Figure 2a,b shows the real and imaginary parts of the dielectric

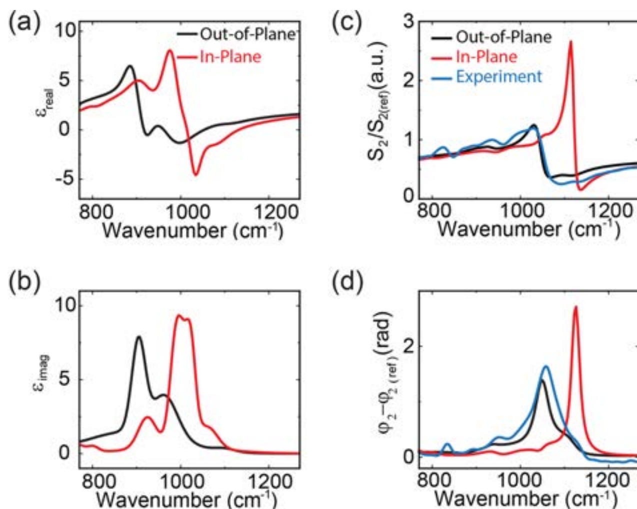

Figure 2. Ellipsometry and nano-FTIR spectra of muscovite mica. Mid-infrared dielectric function is extracted from far-field ellipsometry measurements of muscovite mica. Real (a) and imaginary (b) parts of the permittivity of the in-plane (red curves) and out-of-plane (black) components as a function of excitation frequency are provided. Extended finite dipole model calculation of near-field amplitude S_2 (c) and phase φ_2 (d) spectra performed by using the in-plane (red curves) and out-of-plane (black curves) permittivity. Nano-FTIR experimental spectrum taken on 40 nm mica flake on Si substrate is shown in blue in (c) and (d) for comparison.

functions, respectively, extracted from ellipsometry along the in-plane and out-of-plane directions (with respect to the sample plane). To produce the in-plane component of the dielectric function, we averaged the dielectric data for the in-plane *X*- and *Y*-axes values. This is because the difference between the *X*- and *Y*-axes dielectric data is insignificant (see SI, Figure S2) owing to polycrystalline (with *z*-axis aligned) nature of the sample. The real and imaginary permittivity values plotted in Figure 2 for the in-plane (ε_I, red curve) and out-of-plane (ε_z, black curve) components clearly display anisotropy. Notably, $\mathrm{Re}(\varepsilon_z) < 0$, $\mathrm{Re}(\varepsilon_I) > 0$ in the frequency range 920−1010 cm^{-1} (excluding the range 930−955 cm^{-1}) and $\mathrm{Re}(\varepsilon_I) < 0$, $\mathrm{Re}(\varepsilon_z) > 0$ in the frequency range 1050−1130 cm^{-1}. This implies that mica is a hyperbolic material (Type I in the range 920−1010 cm^{-1} and Type II in the range 1050−1130 cm^{-1}), this is because the in-plane and out-of-plane components of its dielectric permittivity have opposite signs in these frequency ranges. This behavior adds mica to the list of natural hyperbolic materials in the infrared.[21−23] The imaginary parts of the permittivity curves shown in Figure 2b represent dissipation of optical energy accompanying this anomalous optical hyperbolic behavior. These imaginary parts are relatively small in comparison with highly lossy metallic plasmonic materials, but are a factor of 271 at 800 cm^{-1} (Mica $\mathrm{Im}(\varepsilon_z)$/ hBN $\mathrm{Im}(\varepsilon_z)$) and a factor of 32 at 1075 cm^{-1} (Mica $\mathrm{Im}(\varepsilon_z)$/hBN $\mathrm{Im}(\varepsilon_z)$) times larger compared to hBN, another exfoliable hyperbolic material in the infrared.[24,25] We note that the real part of permittivity ratio of mica to hBN is much smaller than the imaginary part ratio (0.38 at 800 cm^{-1} (Mica $\mathrm{Re}(\varepsilon_z)$/ hBN $\mathrm{Re}(\varepsilon_z)$) and a factor of 0.04 at 1075 cm^{-1} (Mica $\mathrm{Re}(\varepsilon_z)$/ hBN $\mathrm{Re}(\varepsilon_z)$) which implies an overdamped system. These experimentally acquired real and imaginary dielectric functions will be used to elucidate near-field spectra and hyperbolic response of mica, the role of thickness and substrate.

When the out-of-plane dielectric function is used in the extended finite dipole model, the calculated spectra fit experimental nano-FTIR spectra very well. This is evident in Figure 2c,d, where the nano-FTIR experimental spectra (blue line) are compared with tip−sample near-field interaction analytical model calculations using the in-plane (red line) and out-of-plane (black line) dielectric data from Figure 2a,b. The normalized near-field nano-FTIR amplitude (Figure 2c) and phase (Figure 2d) spectra were acquired by taking broadband spectra on a 40 nm mica flake and normalized them to a spectra taken at a reference point on the Si substrate surface.[26,27] The calculations were performed by modeling the tip−sample near-field interaction based on a multilayer finite dipole model[28] in which the tip is approximated as an ellipsoid of length of 600 and 30 nm apex radius. The tip is illuminated by the infrared beam at an angle of 30° relative to the sample plane and the scattered signal is collected by the detector, providing amplitude and phase spectra, $s_n(\omega)$ and $\varphi_n(\omega)$[29] via higher-harmonic signal demodulation. The details of the model are presented in the methods section and in refs 26, 28, 30, and 31. The nth harmonic of the electric field component of the scattered light is written as $E_n = S_n e^{i\varphi_n} \propto (1 + r_p)^2 \alpha_{eff}(\beta) E_{inc}$, where r_p is the far-field Fresnel reflection coefficient of the sample,[29] the incident electric field, and $\alpha_{eff}(\beta)$, the effective polarizability,[30] which contains the near-field interaction between tip and sample. The quasi-static near-field reflection coefficient, β, is a function of the frequency-dependent dielectric function, $\varepsilon(\omega)$, of the sample (see Methods for the equation for β with a multilayer model). It is clear from Figure 2c,d that only when the out-of-plane axis dielectric data are used in the calculation that we reproduce the experimental near-field nano-FTIR amplitude and phase spectra. The experimental spectra shown in blue solid lines, amplitude (Figure 2c) and phase (Figure 2d), fit reasonably well with the extended finite dipole model calculations that uses the out-of-plane dielectric data as shown in black solid lines. The model calculations performed using the in-plane dielectric function (red solid lines in Figure 3c,d) significantly deviate from the experimental spectra. This is because light focused on the metalized tip is mainly enhanced along the tip-axis, perpendicular to the sample surface, and probes the sample largely in the out-of-plane direction, which is then scattered by the tip and detected. The small deviation of the theoretical phase spectra from the experiment (Figure 2d) may be due to the tip probing both components (in-plane and out-of-plain) in some proportion instead of exclusively the out-of-plane component, as assumed in the calculation.

In Figure 3a we show representative images of topography and monochromatic s-SNOM amplitude (b, d, and f) and corresponding phase (c, e, and g) images of muscovite mica exfoliated on a Si substrate taken at three selected excitation laser frequencies (1030, 1075, and 1175 cm^{-1}). Additional monochromatic images at several other excitation frequencies are shown in Figure S3. The excitation frequency of 1075 cm^{-1}

https://dx.doi.org/10.1021/acsphotonics.0c00951
ACS Photonics XXXX, XXX, XXX−XXX

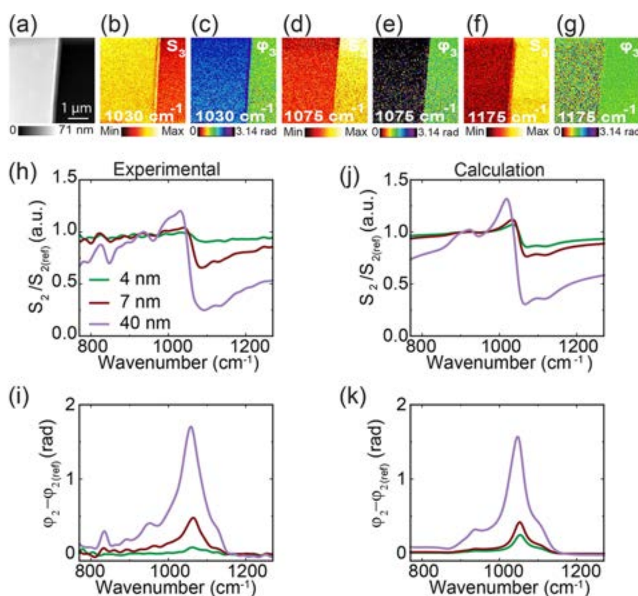

Figure 3. s-SNOM images and nano-FTIR of mica on Si substrate. (a−g) Topography, third harmonic near-field amplitude, and phase images at three different frequencies of 55 nm mica flake on Si. Near-field experimental nano-FTIR amplitude S_2 (h) and phase φ_2 (i) spectra at different thicknesses. Calculated nano-FTIR amplitude S_2 (j) and phase φ_2 (k) spectra.

is of particular interest since it is in the hyperbolic polaritonic range (1050−1130 cm^{-1}) of mica. However, the amplitude/phase images do not display the characteristic interference fringes that are the hallmark of polaritonic propagating modes. We attribute this lack of propagating modes to large losses.[32] The amplitude contrast between mica and Si is inverted at 1030 cm^{-1} due to the large negative Re(ε_1) that enables the normalized amplitude of mica to be larger than unity, whereas wavenumber at 1030 cm^{-1} and larger give mica amplitude contrasts smaller than unity resulting darker profiles than the surrounding Si. To understand the full wavelength and thickness dependent IR optical characteristics, we took nano-FTIR spectra on varying thickness flakes of muscovite mica (thickness ∼ 4, 7, and 40 nm) on a Si substrate. Silicon is a choice substrate for this purpose, since its spectra is featureless in the mid-IR spectral region. In Figure 3h,i we show the experimental normalized amplitude and phase spectra, respectively. Experimentally, these spectra were obtained by normalizing the broadband spectra taken on the mica flake to spectra collected from a reference point on the Si substrate surface.[26,27] The calculation results shown in Figure 3j,k were performed using the extended finite dipole model calculation in which the out-of-plane dielectric function of mica extracted from ellipsometry measurements (as described above) were used to achieve the near-field amplitude and phase spectra of varying thicknesses of muscovite mica exfoliated on Si substrate in the frequency range 750−1300 cm^{-1}. Both the experimental amplitude and phase spectra show similar appearances for different layer thicknesses; however, the signal level becomes progressively smaller with decreasing thickness due to a smaller probed volume. The phase spectra show a prominent broad peak around ∼1080 cm^{-1}. The calculations reproduce the essential features of the experimental amplitude and phase spectra in peak positions and displays thickness dependence signal intensity similar to experimental observations. The broad, strong band between 980 and 1200 cm^{-1} centered around ∼1080 cm^{-1} is due to stretching vibrations of Si−O, which is in better agreement with several reported data.[33−35] The shoulder at 831 cm^{-1} is due to the stretching Al−O mode, whereas the band near 920 cm^{-1} is tentatively assigned as a mixed modes arising from Al−OH stretch, Al−O−Al vibration, and Si−O−Si and Si−O−Al stretching vibrational modes.[33−37]

We took infrared nano-FTIR spectra of heterostructures of various thicknesses of muscovite mica exfoliated on SiO_2. We chose SiO_2 as a supporting substrate because of its strong phonon resonance absorption peak that partially overlaps with mica that may enable phonon−polariton-enhanced IR spectroscopy. In addition, unlike Si, SiO_2 substrate enables facile exfoliation of thin layers of mica down to a monolayer. To investigate the property of hyperbolic modes in mica exfoliated on SiO_2, we took topography (Figure 4a) and near-field amplitude (Figure 4b,d) and the corresponding phase (Figure 4c,e) images at two excitation laser frequencies (1040 and 1175 cm^{-1}). We did not observe propagating modes; however, we observed an enhanced polaritonic signature in the near-field images taken at the hyperbolic spectral range (∼920−1130 cm^{-1}). For example, as shown in Figure 4b, the amplitude and phase images taken at 1040 cm^{-1} show enhanced signal at the topographic steps at different heights, whereas such signatures are lost at 1175 cm^{-1}, which is outside the hyperbolic range (see Figure S4 for more monochromatic images at other excitation frequencies). Similar to the discussion following Figure 3, the absence of clear propagating modes here is also attributed to the weak polaritonic behavior of mica and large losses. In Figure 4f,g we show the experimental amplitude and phase spectra of exfoliated mica down to a monolayer on SiO_2 substrate taken in the IR range (750−1280 cm^{-1}). The

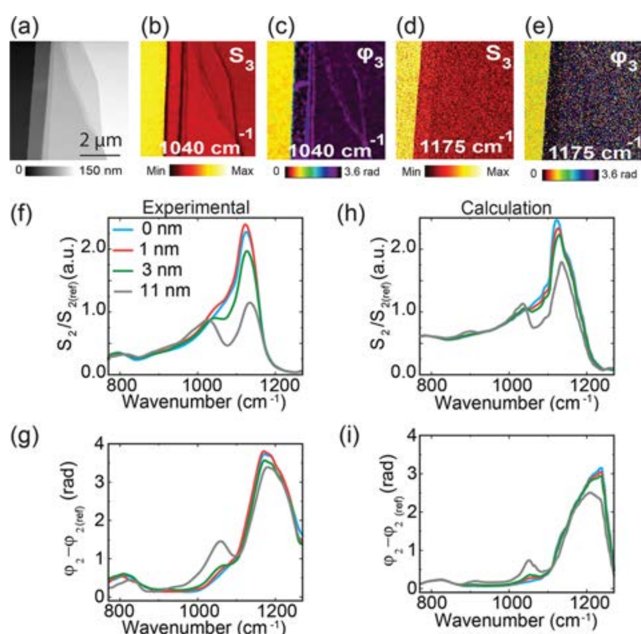

Figure 4. s-SNOM images and nano-FTIR of mica on SiO_2 substrate. (a) Topography image of the mica flake. (c−e) Third harmonic near-field amplitude and phase images of the flake in (a) at two different frequencies. Near-field experimental nano-FTIR amplitude S_2 (f) and phase φ_2 (g) spectra at different thicknesses. Calculated nano-FTIR amplitude S_2 (h) and phase φ_2 (i) spectra.

heterostructure spectra intensity significantly depends on the thickness of the mica layer. As the thickness of the mica decreases, the signal level for all the spectra features arising from the top mica layer (discussed above) progressively decreases, while the known broad peak of SiO_2 centered around ∼1180 cm^{-1} in the phase spectra increases in intensity. We observe a spectral signature of a monolayer thickness. This is evident when comparing the blue and red curves in Figure 4g; the weak shoulder at 1080 cm^{-1} is a clear indication of absorption coming from ∼1 nm thick mica (see Figure S5, zoomed in plots of the phase spectra for 0, 1, and 3 nm for better comparison). This is because of substrate-enhanced absorption due to the combined polaritonic behavior of both mica and SiO_2 in these IR frequency ranges. Furthermore, for a mica flake as thick as 310 nm, we see through it a signature of the SiO_2 spectral signature (see Figure S6), possibly due to the polaritonic behavior of both mica and SiO_2. These experimental trends are reproduced faithfully in intensity changes with thickness and peak positions by the extended finite dipole model calculations (Figure 4h,i) performed using the dielectric function of muscovite mica (as described above) and of SiO_2 from literature.[38]

■ CONCLUSION

We investigated the infrared optical properties of the muscovite monolayer to multilayer mica by a combination of ellipsometry and s-SNOM/nano-FTIR experimental measurements and analytical calculations based on the extended finite dipole method. The dielectric function of muscovite mica in the mid-IR frequencies was extracted from ellipsometry measurements along the in-plane and out-of-plane axes (with respect to the sample plane). These measurements show that mica is a hyperbolic material having the in-plane and out-of-plane components of its dielectric permittivity opposite signs in the IR frequency range 920−1130 cm^{-1}, displaying weak Type I and Type II hyperbolic behavior. Near-field nano-imaging experiments did not find interference fringes of propagating modes expected from polaritonic medium, which may be due to the weak polaritonic behavior of mica and large losses. The extended finite dipole model calculations reproduce the essential features of the experimental amplitude and phase spectra in peak positions and thickness dependence signal intensity when the out-of-plane axis dielectric data is used in the calculations. The prominent broad peak in the phase spectra centered around ∼1080 cm^{-1} is assigned to stretching vibrations of Si−O, and the shoulder peak at 831 cm^{-1} is due to the stretching Al−O mode; the band near 920 cm^{-1} is tentatively assigned as a mixed mode arising from the Al−OH stretch and Al−O−Al, Si−O−Si, and Si−O−Al stretching vibrational modes.

■ METHODS

Extended Finite Dipole Model For Layered Systems. The theoretical approach is based on the finite dipole model and its extension to the layered system in which amplitude (S_n) and phase (φ_n) are calculated by scattered emission:

$$E_n = S_n e^{(i\varphi_n)} \propto (1 + r_p)^2 \alpha_{eff} E_{inc} \quad (1)$$

In eq 1, for mica flake on SiO_2 on Si, r_p is the reflection coefficient for four layers (layer 1 is the surrounding medium, layer 2 is mica with a thickness d_1, layer 3 is SiO_2 with a thickness d_2, and layer 4 is Si) that can be calculated from a multilayer Fresnel reflection coefficient for p-polarized light given by[39,40]

$$r_p(q, \omega) = \frac{r_{12} + r_a \exp(2ik_z(d_1 + d_2))}{1 + r_b \exp(2ik_z(d_1 + d_2))} \quad (2)$$

where r_a and r_b can be calculated as

$$r_a = r_{12}r_{23}r_{34} \exp(-2ik_z d_1) + r_{23} \exp(-2ik_z d_2) + r_{34} \quad (3)$$

$$r_b = r_{23}r_{34} \exp(-2ik_z d_1) + r_{12}r_{23} \exp(-2ik_z d_2) + r_{12}r_{34} \quad (4)$$

r_{ij} is a single interface Fresnel reflection coefficient:[40]

$$r_{ij} = \frac{\varepsilon_j k_{z,i} - \varepsilon_i k_{z,j}}{\varepsilon_j k_{z,i} + \varepsilon_i k_{z,j}} \quad (5)$$

where $k_{z,i} = \sqrt{\varepsilon_i(\omega/c)^2 - q^2}$.[41] In eq 1, α_{eff} is the effective polarizability. Equations 6−15 give us the effective polarizability, which is described in ref 30. L is the effective length of the tip, R_t is the tip curvature radius, which is 20 nm, C is the height-independent constant with $Q_0 = R_t^2 E_0$, which is the total amount of the polarization charge induced in the tip in the absence of sample, which is described in ref 28, and H is the tip and sample distance.

$$\alpha_{eff} = C\left(1 + \frac{1}{2}\frac{f_0(H)\beta(\varepsilon)}{1 - f(H)\beta(\varepsilon)}\right) \quad (6)$$

$$f_0(H) = \left(g - \frac{2H + W_0 + R_t}{2L}\right)\frac{\ln\frac{4L}{4H + 2W_0 + R_t}}{\ln\frac{4L}{R_t}} \quad (7)$$

$$f(H) = \left(g - \frac{2H + W_i + R_t}{2L}\right)\frac{\ln\frac{4L}{4H + 2R_t}}{\ln\frac{4L}{R_t}} \quad (8)$$

$$C = L\frac{Q_0}{|E_0|} \quad (9)$$

$$W_0 \approx 1.31R_tL/(L + 2R_t) \quad (10)$$

$$W_i \approx R_t/2 \quad (11)$$

β is the quasi-static, near-field reflection coefficient given by[39]

$$\beta = \frac{\beta_{12} + \beta_a \exp(-2q(d_1 + d_2))}{1 + \beta_b \exp(-2q(d_1 + d_2))} \quad (12)$$

where β_a and β_b can defined as

$$\beta_a = \beta_{12}\beta_{23}\beta_{34} \exp(2qd_1) + \beta_{23} \exp(2qd_2) + \beta_{34} \quad (13)$$

$$\beta_b = \beta_{23}\beta_{34} \exp(2qd_1) + \beta_{12}\beta_{23} \exp(2qd_2) + \beta_{12}\beta_{34} \quad (14)$$

The electrostatic reflection coefficient β_{ij} is defined by[39]

$$\beta_{ij} = \frac{\varepsilon_j - \varepsilon_i}{\varepsilon_j + \varepsilon_i} \quad (15)$$

For further comparisons and details on the finite dipole model and the extended finite dipole model for layered systems, see the SI.

https://dx.doi.org/10.1021/acsphotonics.0c00951
ACS Photonics XXXX, XXX, XXX−XXX

■ ASSOCIATED CONTENT

Supporting Information

The Supporting Information is available free of charge at https://pubs.acs.org/doi/10.1021/acsphotonics.0c00951.

Permittivity for different in-plane axes, near-field images of mica/Si, near-field images of mica/SiO_2, zoomed in nano-FTIR spectra of different thicknesses of mica, and nano-FTIR amplitude and phase thickness of mica (PDF)

■ AUTHOR INFORMATION

Corresponding Author

Yohannes Abate − *Department of Physics and Astronomy, University of Georgia, Athens, Georgia 30602-2451, United States*; orcid.org/0000-0003-1313-1766; Email: yohannes.abate@uga.edu

Authors

Alireza Fali − *Department of Physics and Astronomy, University of Georgia, Athens, Georgia 30602-2451, United States*

Sampath Gamage − *Department of Physics and Astronomy, University of Georgia, Athens, Georgia 30602-2451, United States*

Marquez Howard − *Department of Physics and Astronomy, University of Georgia, Athens, Georgia 30602-2451, United States*

Thomas. G. Folland − *Department of Mechanical Engineering, Vanderbilt University, Nashville, Tennessee 37212, United States*; orcid.org/0000-0002-4665-235X

Nadeemullah A. Mahadik − *U.S. Naval Research Laboratory, Washington, D.C. 20375, United States*

Tom Tiwald − *J. A. Woollam Co., Inc., Lincoln, Nebraska 68508, United States*

Kirill Bolotin − *Institute of Experimental Physics, Freie Universität Berlin, Berlin 14195, Germany*

Joshua D. Caldwell − *Department of Mechanical Engineering, Vanderbilt University, Nashville, Tennessee 37212, United States*; orcid.org/0000-0003-0374-2168

Complete contact information is available at: https://pubs.acs.org/10.1021/acsphotonics.0c00951

Funding

A.F. acknowledges support from the National Science Foundation, Grant No. 1553251. Y.A. and M.H. acknowledge support from the Air Force Office of Scientific Research, Grant No. FA9559-16-1-0172. K.B. acknowledges funding by ERC Starting Grant No. 639739 and NSF DMR 1508433.

Notes

The authors declare no competing financial interest.

■ REFERENCES

(1) Geim, A. K.; Novoselov, K. S. The rise of graphene. *Nat. Mater.* **2007**, *6*, 183−191.

(2) Xu, M.; Liang, T.; Shi, M.; Chen, H. Graphene-Like Two-Dimensional Materials. *Chem. Rev.* **2013**, *113*, 3766−3798.

(3) Jariwala, D.; Sangwan, V. K.; Lauhon, L. J.; Marks, T. J.; Hersam, M. C. Emerging Device Applications for Semiconducting Two-Dimensional Transition Metal Dichalcogenides. *ACS Nano* **2014**, *8*, 1102−1120.

(4) Rickwood, P. C. The largest crystals. *Am. Mineral.* **1981**, *66*, 885−907.

(5) de Poel, W.; Pintea, S.; Drnec, J.; Carla, F.; Felici, R.; Mulder, P.; Elemans, J. A. A. W.; van Enckevort, W. J. P.; Rowan, A. E.; Vlieg, E. Muscovite mica: Flatter than a pancake. *Surf. Sci.* **2014**, *619*, 19−24.

(6) Jia, F.; Song, S. Preparation of monolayer muscovite through exfoliation of natural muscovite. *RSC Adv.* **2015**, *5*, 52882−52887.

(7) Castellanos-Gomez, A.; Wojtaszek, M.; Tombros, N.; Agraït, N.; van Wees, B. J.; Rubio-Bollinger, G. Atomically Thin Mica Flakes and Their Application as Ultrathin Insulating Substrates for Graphene. *Small* **2011**, *7*, 2491−2497.

(8) Osman, M. A.; Caseri, W. R.; Suter, U. W. H+/Li+and H+/K +Exchange on Delaminated Muscovite Mica. *J. Colloid Interface Sci.* **1998**, *198*, 157−163.

(9) de Poel, W.; Vaessen, S. L.; Drnec, J.; Engwerda, A. H. J.; Townsend, E. R.; Pintea, S.; de Jong, A. E. F.; Jankowski, M.; Carlà, F.; Felici, R.; Elemans, J. A. A. W.; van Enckevort, W. J. P.; Rowan, A. E.; Vlieg, E. Metal ion-exchange on the muscovite mica surface. *Surf. Sci.* **2017**, *665*, 56−61.

(10) Akutagawa, T.; Ohta, T.; Hasegawa, T.; Nakamura, T.; Christensen, C. A.; Becher, J. Formation of oriented molecular nanowires on mica surface. *Proc. Natl. Acad. Sci. U. S. A.* **2002**, *99*, 5028−5033.

(11) Kankate, L.; Balzer, F.; Niehus, H.; Rubahn, H.-G. From clusters to fibers: Parameters for discontinuous para-hexaphenylene thin film growth. *J. Chem. Phys.* **2008**, *128*, No. 084709.

(12) de Poel, W.; Pintea, S.; de Jong, A.; Drnec, J.; Carlà, F.; Felici, R.; op den Camp, H.; Elemans, J. A. A. W.; van Enckevort, W. J. P.; Rowan, A. E.; Vlieg, E. Dibenzo Crown Ether Layer Formation on Muscovite Mica. *Langmuir* **2014**, *30*, 12570−12577.

(13) Pintea, S.; de Poel, W.; de Jong, A. E. F.; Vonk, V.; van der Asdonk, P.; Drnec, J.; Balmes, O.; Isern, H.; Dufrane, T.; Felici, R.; Vlieg, E. Solid−Liquid Interface Structure of Muscovite Mica in CsCl and RbBr Solutions. *Langmuir* **2016**, *32*, 12955−12965.

(14) Simbrunner, C.; Hernandez-Sosa, G.; Quochi, F.; Schwabegger, G.; Botta, C.; Oehzelt, M.; Salzmann, I.; Djuric, T.; Neuhold, A.; Resel, R.; Saba, M.; Mura, A.; Bongiovanni, G.; Vollmer, A.; Koch, N.; Sitter, H. Color Tuning of Nanofibers by Periodic Organic−Organic Hetero-Epitaxy. *ACS Nano* **2012**, *6*, 4629−4638.

(15) Crow, M. L. Characterization of mica crystals as reflectors for an ultracold neutron doppler converter. *Phys. B* **1997**, *241−243*, 110−112.

(16) Li, L.; Lu, G.; Li, S.; Tang, H.; Yang, X. Epitaxy-Assisted Creation of PCBM Nanocrystals and Its Application in Constructing Optimized Morphology for Bulk-Heterojunction Polymer Solar Cells. *J. Phys. Chem. B* **2008**, *112*, 15651−15658.

(17) Jellison, G. E. Data analysis for spectroscopic ellipsometry. *Thin Solid Films* **1993**, *234*, 416−422.

(18) Tompkins, H. G.; Irene, E. A. *Handbook of Ellipsometry*; William Andrew Publishing, 2005; pp 3−540.

(19) Jellison, G. E. Data Analysis for Spectroscopic Ellipsometry. In *Handbook of Ellipsometry*; Tompkins, H. G., Irene, E. A., Eds.; William Andrew Publishing: Norwich, NY, 2005; pp 237−296.

(20) Herzinger, C. M.; Snyder, P. G.; Johs, B.; Woollam, J. A. InP optical constants between 0.75 and 5.0 eV determined by variable-angle spectroscopic ellipsometry. *J. Appl. Phys.* **1995**, *77*, 1715−1724.

(21) Caldwell, J. D.; Kretinin, A. V.; Chen, Y.; Giannini, V.; Fogler, M. M.; Francescato, Y.; Ellis, C. T.; Tischler, J. G.; Woods, C. R.; Giles, A. J.; Hong, M.; Watanabe, K.; Taniguchi, T.; Maier, S. A.; Novoselov, K. S. Sub-diffractional volume-confined polaritons in the natural hyperbolic material hexagonal boron nitride. *Nat. Commun.* **2014**, *5*, 5221.

(22) Ma, W.; Alonso-González, P.; Li, S.; Nikitin, A. Y.; Yuan, J.; Martín-Sánchez, J.; Taboada-Gutiérrez, J.; Amenabar, I.; Li, P.; Vélez, S.; Tollan, C.; Dai, Z.; Zhang, Y.; Sriram, S.; Kalantar-Zadeh, K.; Lee, S.-T.; Hillenbrand, R.; Bao, Q. In-plane anisotropic and ultra-low-loss polaritons in a natural van der Waals crystal. *Nature* **2018**, *562*, 557−562.

(23) Narimanov, E. E.; Kildishev, A. V. Naturally hyperbolic. *Nat. Photonics* **2015**, *9*, 214−216.

509 (24) Caldwell, J. D.; Lindsay, L.; Giannini, V.; Vurgaftman, I.;
510 Reinecke, T. L.; Maier, S. A.; Glembocki, O. J. Low-loss, infrared and
511 terahertz nanophotonics using surface phonon polaritons. *Nano-*
512 *photonics* **2015**, *4*, 44−68.
513 (25) Basov, D. N.; Fogler, M. M.; García de Abajo, F. J. Polaritons in
514 van der Waals materials. *Science* **2016**, *354*, aag1992.
515 (26) Huth, F.; Govyadinov, A.; Amarie, S.; Nuansing, W.; Keilmann,
516 F.; Hillenbrand, R. Nano-FTIR Absorption Spectroscopy of
517 Molecular Fingerprints at 20 nm Spatial Resolution. *Nano Lett.*
518 **2012**, *12*, 3973−3978.
519 (27) Stiegler, J. M.; Abate, Y.; Cvitkovic, A.; Romanyuk, Y. E.;
520 Huber, A. J.; Leone, S. R.; Hillenbrand, R. Nanoscale Infrared
521 Absorption Spectroscopy of Individual Nanoparticles Enabled by
522 Scattering-Type Near-Field Microscopy. *ACS Nano* **2011**, *5*, 6494−
523 6499.
524 (28) Cvitkovic, A.; Ocelic, N.; Hillenbrand, R. Analytical model for
525 quantitative prediction of material contrasts in scattering-type near-
526 field optical microscopy. *Opt. Express* **2007**, *15*, 8550−8565.
527 (29) Zhang, L. M.; Andreev, G. O.; Fei, Z.; McLeod, A. S.;
528 Dominguez, G.; Thiemens, M.; Castro-Neto, A. H.; Basov, D. N.;
529 Fogler, M. M. Near-field spectroscopy of silicon dioxide thin films.
530 *Phys. Rev. B: Condens. Matter Mater. Phys.* **2012**, *85*, No. 075419.
531 (30) Govyadinov, A. A.; Amenabar, I.; Huth, F.; Carney, P. S.;
532 Hillenbrand, R. Quantitative Measurement of Local Infrared
533 Absorption and Dielectric Function with Tip-Enhanced Near-Field
534 Microscopy. *J. Phys. Chem. Lett.* **2013**, *4*, 1526−1531.
535 (31) Aghamiri, N. A.; Huth, F.; Huber, A. J.; Fali, A.; Hillenbrand,
536 R.; Abate, Y. Hyperspectral time-domain terahertz nano-imaging. *Opt.*
537 *Express* **2019**, *27*, 24231−24242.
538 (32) Fali, A.; White, S. T.; Folland, T. G.; He, M.; Aghamiri, N. A.;
539 Liu, S.; Edgar, J. H.; Caldwell, J. D.; Haglund, R. F.; Abate, Y.
540 Refractive Index-Based Control of Hyperbolic Phonon-Polariton
541 Propagation. *Nano Lett.* **2019**, *19*, 7725−7734.
542 (33) Zhang, M.; Redfern, S. A. T.; Salje, E. K. H.; Carpenter, M. A.;
543 Hayward, C. L. Thermal behavior of vibrational phonons and
544 hydroxyls of muscovite in dehydroxylation: In situ high-temperature
545 infrared spectroscopic investigations. *Am. Mineral.* **2010**, *95*, 1444−
546 1457.
547 (34) Beran, A., Crystal Chemistry and Metamorphic Petrology. In
548 *Infrared Spectroscopy of Micas*; Mottana, A., Sassi, F. P., Thompson, J.
549 B., Guggenheim, S., Eds.; De Gruyter, 2002; Vol. *46*, pp 351−369.
550 (35) Smrčok, L. u.; Rieder, M.; Kolesnikov, A. I.; Granroth, G. E.
551 Combined inelastic neutron scattering and solid-state density
552 functional theory study of dynamics of hydrogen atoms in muscovite
553 $2M_1$. *Am. Mineral.* **2011**, *96*, 301−307.
554 (36) Singha, M.; Singh, L. Vibrational spectroscopic study of
555 muscovite and biotite layered phyllosilicates. *Indian J. Pure Appl. Phys.*
556 **2016**, 116−122.
557 (37) Redhammer, G. n. J.; Beran, A.; Schneider, J.; Amthauer, G.;
558 Lottermoser, W. Spectroscopic and structural properties of synthetic
559 micas on the annite-siderophyllite binary: Synthesis, crystal structure
560 refinement, Mössbauer, and infrared spectroscopy. *Am. Mineral.* **2000**,
561 *85*, 449−465.
562 (38) Kischkat, J.; Peters, S.; Gruska, B.; Semtsiv, M.; Chashnikova,
563 M.; Klinkmüller, M.; Fedosenko, O.; Machulik, S.; Aleksandrova, A.;
564 Monastyrskyi, G.; Flores, Y.; Ted Masselink, W. Mid-infrared optical
565 properties of thin films of aluminum oxide, titanium dioxide, silicon
566 dioxide, aluminum nitride, and silicon nitride. *Appl. Opt.* **2012**, *51*,
567 6789−6798.
568 (39) Hauer, B.; Engelhardt, A. P.; Taubner, T. Quasi-analytical
569 model for scattering infrared near-field microscopy on layered
570 systems. *Opt. Express* **2012**, *20*, 13173−13188.
571 (40) Mastel, S.; Govyadinov, A. A.; de Oliveira, T. V. A. G.;
572 Amenabar, I.; Hillenbrand, R. Nanoscale-resolved chemical identi-
573 fication of thin organic films using infrared near-field spectroscopy
574 and standard Fourier transform infrared references. *Appl. Phys. Lett.*
575 **2015**, *106*, No. 023113.
576 (41) McLeod, A. S.; Kelly, P.; Goldflam, M. D.; Gainsforth, Z.;
577 Westphal, A. J.; Dominguez, G.; Thiemens, M. H.; Fogler, M. M.;
Basov, D. N. Model for quantitative tip-enhanced spectroscopy and 578
the extraction of nanoscale-resolved optical constants. *Phys. Rev. B:* 579
Condens. Matter Mater. Phys. **2014**, *90*, No. 085136. 580